

Re-Evaluating LiDAR Scene Flow for Autonomous Driving

Nathaniel Chodosh¹ Deva Ramanan¹ Simon Lucey²

¹Carnegie Mellon University ²University of Adelaide

nchodosh@andrew.cmu.edu deva@cs.cmu.edu simon.lucey@adelaide.edu.au

Abstract

Current methods for self-supervised LiDAR scene flow estimation work poorly on real data. A variety of flaws in common evaluation protocols have caused leading approaches to focus on problems that do not exist in real data. We analyze a suite of recent works and find that despite their focus on deep learning, the main challenges of the LiDAR scene flow problem – removing the dominant rigid motion and robustly estimating the simple motions that remain – can be more effectively solved with classical techniques such as ICP motion compensation and enforcing piecewise rigid assumptions. We combine these steps with a test-time optimization method to form a state-of-the-art system that does not require any training data. Because our final approach is dataless, it can be applied on different datasets with diverse LiDAR rigs without retraining. Our proposed approach outperforms all existing methods on Argoverse 2.0, halves the error rate on NuScenes, and even rivals the performance of supervised networks on Waymo and lidarKITTI.

1. Introduction

Research is often guided by improving benchmark results, but popular scene flow benchmarks are guiding research in the wrong direction. Scene flow, the 3D analog of optical flow [71], can help autonomous vehicles identify moving objects around them. Most autonomous vehicle platforms use LiDAR sensors for direct 3D perception, creating interest in estimating scene flow between successive LiDAR scans [45, 7]. If this task can be accomplished without relying on labeled data, it can give autonomous vehicles awareness of moving objects even if they are outside the detection taxonomy [79, 52, 5]. We focus on this self-supervised setting and show that the standard benchmarks have several fundamental flaws. When evaluated more realistically, apparent benchmark improvements correspond to stalled or even decreasing real-world performance (Fig. 1).

Most work follows the evaluation framework from FlowNet3D [45], which primarily measures the average

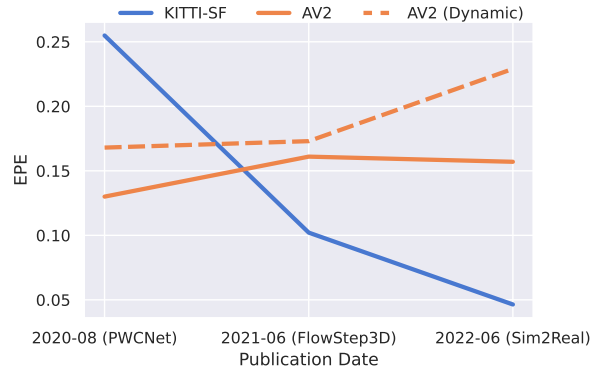


Figure 1. The performance of top self-supervised models (PPWC, FlowStep3D, Sim2Real) as a function of their publication date. (Blue) shows self-reported performance on KITTI-SF and (red) shows results on Argoverse 2.0, separated into all points (solid) and only dynamic points (dashed). As can be seen, progress on the synthetic KITTI-SF benchmark leads to worse performance on real data, particularly on dynamic points.

end-point-error (EPE) across FlyingThings3D [48] and KITTI-SF [50]. This leads to several issues: (1) KITTI-SF samples dynamic objects with an artificial pattern that differs from the pattern on static objects, inadvertently providing part of the “answer” to learning-based approaches (Fig. 2). (2) Both FlyingThings3D and KITTI-SF ensure successive point clouds are in one-to-one correspondence, which is never the case for real data. (3) Both datasets contain an unrealistically high percentage of dynamic points. In contrast, real-world data is dominated by the background.

Together these issues obfuscate the main challenges of LiDAR scene flow, which are identifying the few non-static points and estimating their motions robustly given the lack of correspondences. We demonstrate the impact of these issues by evaluating a suite of top methods on a new LiDAR scene flow benchmark, finding that performance on this real-world data does not correlate with performance on the standard benchmarks.

We propose addressing these main difficulties with classical techniques: ICP for removing the dominant ego-motion, and robust motion estimation through RANSAC

fitting of piecewise rigid models. We pose these as pre- and post-processing steps around a test-time optimization method for estimating non-rigid flow, creating a completely dataless approach. Nevertheless, we show that our proposed method outperforms the state of the art by a wide margin on Argoverse, NuScenes [48] and lidarKITTI [20], as well as even outperforming or rivaling supervised networks on Waymo.

In summary, our main contributions are:

- An investigation of the weakness of current self-supervised scene flow evaluations.
- A new large-scale scene flow benchmark that addresses the aforementioned weakness along with a thorough evaluation of existing approaches¹.
- A *dataless* flow method which gives state-of-the-art results.

2. Related Work

Scene Flow: Scene flow was introduced by [72], who posed the problem in the stereo RGB setting and spawned a large body of subsequent work [3, 10, 22, 25, 23, 49, 59, 58, 74, 75]. A related problem is non-rigid registration [1, 13, 40, 28, 57], which is focused on fitting dense point clouds or meshes. We are interested in the setting without images, based purely on sparse LiDAR point clouds.

Optimization based LiDAR Scene Flow: Dataless LiDAR scene flow estimation was first proposed by Dewan *et al.* [14]. Inspired by a non-rigid registration method regularized by the graph Laplacian [16], Pontes *et al.* [60] created an improved method. Their results were further improved upon by Li *et al.* [43] with the implicit regularization of coordinate networks [2, 11, 51, 56, 68]. We use [43] as the backbone of our method and additionally employ coordinate networks for height-map estimation. Najibi *et al.* [54] proposed extensions to the method of Li *et al.* as a part of a meta-labeling pipeline. These extensions are similar to ours in that they also remove static points and make use of clustering. However, they rely on multiple scans for the former and do not make use of rigid motion priors for the latter. Direct comparisons with their method are difficult as they do not provide an implementation or results on open benchmarks.

Learning Based LiDAR Scene Flow: Originally, deep learning scene flow methods used convolutional neural networks to fuse RGB and depth information [8, 64, 67, 48, 69], with some work focusing specifically on the challenges of autonomous driving [27, 30, 47, 65, 66]. PointNet and related techniques [62, 63, 44] enabled a shift to point cloud scene flow estimation beginning with FlowNet3D and

¹Weights and outputs for all the evaluated methods will also be released along with the *processed* dataset with labels

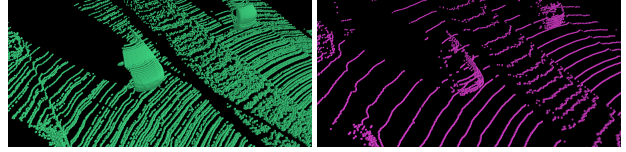


Figure 2. Comparison of sampling patterns from KITTI-SF (**left**) versus the corresponding real LiDAR scan (**right**). KITTI-SF uses dense CAD models for foreground objects, which makes it easier for learning-based methods to find them among the sparse LiDAR background points.

PointFlowNet [45, 7]. Many works followed, exploring different architectures and losses [70, 37, 79, 20, 21, 4, 61, 41, 77, 33, 12, 76]. Particularly notable examples are PointPWC [79] which introduced a cost-volume formulation, FLOT [61] which posed the problem in terms of estimating weights for optimal transport, HPLFlowNet [21] which transformed the input to a permutohedral lattice to enable more traditional convolutional architectures, and FastFlowNet [33] which built on the PointPillars [38] architecture. However, we are focused on methods that can leverage unlabeled LiDAR data.

Self and Weakly-Supervised LiDAR Scene Flow: “Just Go with the Flow” [52] demonstrated that using a combination of nearest-neighbor and cycle consistency losses was enough to train the FlowNet3D network, avoiding the reliance on labeled data. This led to many other works which adopted similar losses [79, 70, 37, 5]. Others made use of easier to acquire sources of supervision such as foreground/background segmentation masks [20, 15] or addressed the synthetic to real domain gap [32]. We demonstrate superior performance without using any labels. Of particular relevance are those methods which make use of ego-motion estimation and piecewise rigid representations [20, 15, 42]. We adopt some similar components but show that in real-world data, ICP vastly outperforms learned approaches and that piecewise rigidity is more effective when used to find inliers rather than as a loss regularizer. Unlike [42] we do not require many rounds of costly supervised training on pseudo-labels.

Ground Segmentation: In robotics, ground segmentation has been studied as a subset of general dataless segmentation [53], traversable area identification [24], and as a pre-processing step for object detection, classification and tracking [80, 55, 31, 39]. Current scene flow methods do not make use of these sophisticated methods and instead rely on basic plane fitting [5, 21, 54]. In order to show how even small improvements to pre- and post- processing steps can drastically improve scene flow estimation, we propose a simple segmentation method based on coordinate networks.

2.1. Self-Supervised LiDAR Flow Evaluation

Most self-supervised flow estimation works inherit their evaluation protocol from [45], which is based on the synthetic FlyingThings3D [48] and KITTI-SF [50, 19]. Both were created for evaluating RGB-based flow methods and [45] extended them to point clouds by lifting the optical flow and depth annotations to 3D. These datasets and protocols suffer from several deficiencies which present specific issues for self-supervised methods.

One-to-One Correspondence: Since both FlyingThings3D and KITTI-SF are created by lifting optical flow annotations, the point clouds for each input pair are in one-to-one correspondence. That is, for each 3D point p_i and ground truth 3D flow f_i in the first frame, there exists a 3D point q_i in the second frame such that $p_i + f_i = q_i$. Real-world LiDAR scans do not have this property and given their sparsity often violate it, especially at range. The presence of correspondences fundamentally changes the LiDAR scene flow problem into a different point matching problem. It has been claimed that randomly sub-sampling the input breaks this correspondence. However, given the total number of points in each scan (90k) and the number of sub-sampled points (8192), there are still an expected 745 corresponding points in the input. Since each example has a handful of independent motions, these correspondences are enough to constrain the solution.

Number of Dynamic Points: In any scene some portion of the measured points belong to the static background rather than dynamically moving objects. In real-world LiDAR scans such as those in NuScenes [9], Waymo [33], or Argoverse 2 [78], the percentage of static points is very high, ranging from 85-100%. In contrast, FlyingThings3D has 0% static points since it consists of flying things, and the KITTI-SF dataset has approximately 60% static points [5]. Dealing with this data imbalance is one of the key difficulties of self-supervised flow estimation but it is not present in the popular benchmarks.

Dynamic Sampling Pattern: The ground truth flow and disparity of KITTI-SF were created by fitting 3D models to the LiDAR points and 2D annotations [49]. This gives the dynamic objects a distinctive dense sampling pattern that separates them from the background (see Fig. 2). As discussed above, determining which points belong to moving objects is one of the main challenges and the sampling pattern effectively gives away the answer in the input. A learning-based system can simply identify moving objects by the pattern without learning anything about the motion (see supplemental material).

Due to these deficiencies, recent works have made progress on improving results on these benchmarks without improving results on real-world data (Fig. 1). Some of the problems could perhaps be addressed through resampling, but doing so requires modifying the data based on

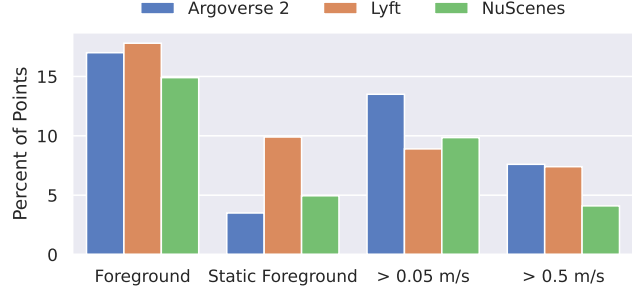


Figure 3. An analysis of the motion profile of points found in various autonomous driving datasets. The leftmost column is the percentage of points belonging to any tracked object. The right three columns show those points separated by their speed once ego-motion has been removed.

Dataset	Scenes	Avg Points	Frames
Waymo	1150	177000	198000
NuScenes	889	25000	33000
Lyft	350	60000	30000
lidarKITTI	29	15000	142
Argoverse 2	850	83000	132000

Table 1. Comparison of scene flow datasets in terms of the number of scenes, the average number of LiDAR points per frame, and the number of frames

the ground truth static-vs-dynamic labels. This runs counter to the goal of creating methods that operate on raw, unlabeled data.

Some works have evaluated on real LiDAR data by transferring synthetic labels [20], or more commonly by computing flows from object-level tracks [5, 33, 32, 43]. However, those evaluations have been presented as auxiliary results [5, 43] with limited comparisons to existing methods, or without comparison entirely [33]. As a result, KITTI-SF and FlyingThing3D remain the standard benchmarks. We argue that evaluating on real-data should be the “gold-standard” for scene flow as opposed to synthetic benchmarks. To this end, we create and release a new large-scale LiDAR scene flow benchmark, train and release a suite of top methods on it, and show that good performance on synthetic data does not correspond to good performance on LiDAR data. Additionally, we show results on all existing LiDAR benchmarks in order to encourage their use as well.

3. Scene Flow Benchmark

We use the pseudo-labeling method found in [5, 33, 32, 43] to generate labels from object-level tracks found in various large-scale multi-object tracking (MOT) datasets.

Problem Statement: We assume as input two point clouds $\mathbf{P}^t \in \mathbb{R}^{N \times 3}, \mathbf{P}^{t+\Delta} \in \mathbb{R}^{M \times 3}$. The superscript indicates that these point clouds are separated by a small time delta (usually $\Delta = 0.1$ s), and the variables N, M indicate that the two point clouds have different numbers of points. The goal is to predict a set of flow vectors $\{\mathbf{f}_i \in \mathbb{R}^3\}_{i=1}^N$

which describe the motion of each point from time t to time $t + \Delta$. Some datasets also give access to the ego-motion of the sensor since in the autonomous vehicle setting this information is available from odometry or GPS.

Flow Label Creation: For each point cloud in a MOT dataset we have a set of oriented bounding boxes $\{B_i^t\}_{i=1}^K$. For each B_i^t , if the second frame at time $t + \Delta$ contains a corresponding bounding box $B_j^{t+\Delta}$, we can extract the rigid transformation $\mathbf{R}_i^t, \mathbf{t}_i^t$ that transforms points in the first box to the second. For each point \mathbf{p}_j inside the bounding box we assign it the flow $\mathbf{f}_j = \mathbf{R}_i \mathbf{p}_j + \mathbf{t}_i$. Points not belonging to any bounding box are assigned the ego-motion as flow. For objects which only appear in one frame, we cannot compute the ground truth flow and so they are ignored for evaluation purposes but included in the input.

Limitations: This procedure for producing flow labels has two drawbacks. First is that all the points inside a bounding box may not be moving rigidly. While it is important to be aware of this we believe the errors introduced are small since most objects are rigid vehicles and the sampling rate of 10Hz prevents large deviations from the model. Second, there can exist objects that are not captured by the tracking labels but are nonetheless dynamic. This second limitation is the main reason for our interest in self- and un-supervised methods as existing work has demonstrated degradation of supervised performance on objects not included in the training labels [33]. However, it is supervised training that creates the correlation between performance on an object class and its presence in the labels. For self-supervised methods we expect performance on tracked objects to correlate with those that may be missing.

Base Dataset Choice: The described label creation procedure can be applied to any multi-object tracking dataset. Therefore it is worthwhile to determine what base tracking dataset will produce the best benchmark. The options are NuScenes [9], Lyft Perception [35], Waymo [33], and Argoverse 2.0 [78]. First, we eliminate Waymo since its licensing disallows the release of trained models, forcing researchers to replicate expensive training procedures. Flow labels for NuScenes and Lyft have already been created, and we evaluate on the NuScenes benchmark [5]. We omit the Lyft benchmark [32] as much of the input points have been discarded to match the FOV of the synthetic data introduced alongside it. Regardless, Fig. 3 and Tab. 1 show that Argoverse 2.0 has more scenes, points-per-scene, and dynamic objects than either existing dataset. Additionally, we subjectively see fewer labeling errors in Argoverse as compared to NuScenes. Therefore we chose it as the basis of a new benchmark.

4. Method

Our pipeline (Fig. 4), consists mainly of pre- and post-processing steps around the test-time flow optimization

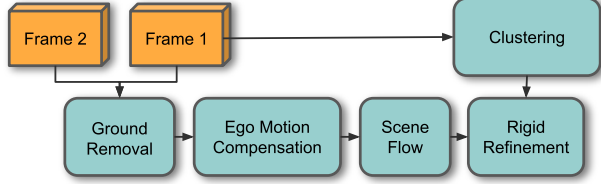


Figure 4. Our proposed pipeline for LiDAR scene flow based largely on classical pre- and post-processing.

method of [43].

Motion Compensation: Since real-world scenes consist mostly of static background objects, removing the ego-motion of the sensor makes estimating the dynamic motion significantly easier (Fig. 5). For benchmarks such as Argoverse or Waymo, the ego-motion is provided and we transform the first scan into the coordinate frame of the second.

NuScenes and lidarKITTI also have this information but previous work has opted to not use it. In this case, we use ICP [10, 73] to first estimate the ego-motion. We demonstrate experimentally that this is much more effective than learned approaches. **Ground Removal:** The sampling pattern of a LiDAR sensor creates “swimming” artifacts as the sensor moves. These artifacts create the appearance of motion and present a large problem for the nearest neighbor loss function used by almost all self-supervised methods. The largest artifacts come from the ground, leading most methods to remove them by height thresholding or by fitting a plane [5, 45]. This can fail when the ground changes elevation either from hills or even sidewalks, see Fig. 6. We propose an improvement based on analyzing the assumptions behind the current approaches. These assumptions are:

1. The sensor has been calibrated such that the ground can be represented as a height map $h = f(x, y)$.
2. Except for a small number of noise returns, all measured points (x, y, z) satisfy $z \geq f(x, y)$
3. The ground function $f(x, y)$ is in some way “simple”. Existing methods make use of this assumption by requiring $f(x, y) = c$ for thresholding or $f(x, y) = ax + by + c$ for plane fitting.

The issue comes from an overly strict application of assumption (3). Instead, we allow our height map to be *piecewise linear* rather than linear. To represent our piecewise linear height map we use a 3-layer coordinate network with ReLU activations and 64 hidden units per layer. To fit it we use assumption (2) to design a one-sided robust loss:

$$\mathcal{L}_{height}(h, z) = \begin{cases} (h - z)^2 & z < h \\ \text{Huber}(h, z) & h \leq z \end{cases}. \quad (1)$$

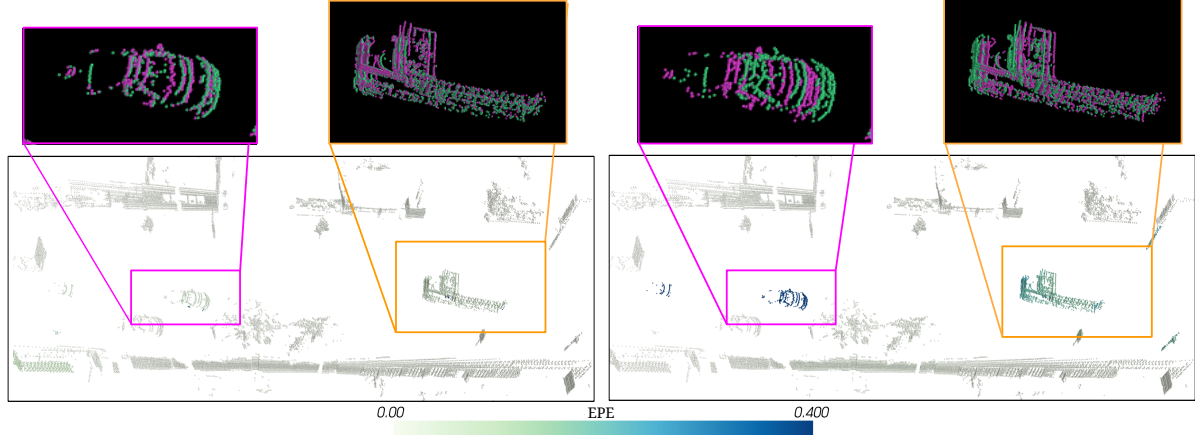


Figure 5. Comparison between NSFP with our proposed pre and post processing steps (**left**) and standard NSFP (**right**). In the (**bottom**) views points are color coded by EPE. The (**top**) detail views show the first and second frames aligned by the predicted flow. NSFP struggles to represent both foreground and background motion. We find that first using ICP to remove ego-motion greatly improves the estimates on dynamic points.

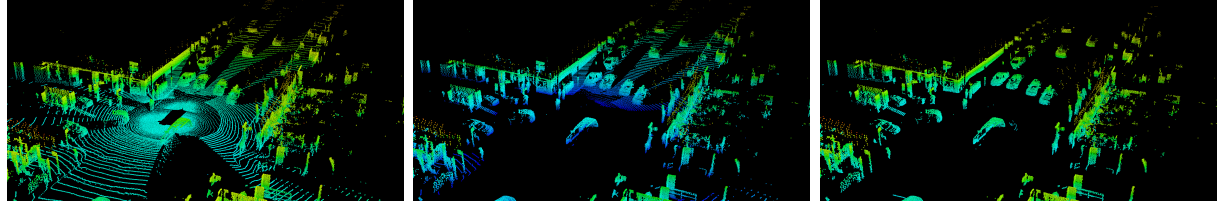


Figure 6. An example of our ground removal technique on a Waymo [33] scene with a non-planar ground. In all images, color coding indicates the height of each point. From left to right: the input point cloud, the result of thresholding, our result.

The Huber function [26] allows the network to ignore points high above the ground. For each point cloud the parameters of our height-map θ_h are found by optimizing

$$\min_{\theta_h} \sum_{i=1}^N \mathcal{L}_{height}(f_{\theta_h}(x_i, y_i), z_i). \quad (2)$$

Finally, any points which are less than 0.3m above our predicted ground are removed.

Scene Flow Estimation: Once the ego-motion and ground points have been removed, we estimate the scene flow using the method of Li *et al.* [43]. Briefly, this means that we represent the forwards and backward flow using two coordinate networks $f_{\theta_{fw}}, f_{\theta_{bw}} \in \mathbb{R}^{N \times 3} \rightarrow \mathbb{R}^{N \times 3}$ which are optimized with gradient descent on the objective:

$$\min_{\theta_{fw}, \theta_{bw}} \mathcal{C}(g_{\theta_{fw}}(\mathbf{P}^t), \mathbf{P}^{t+\Delta}) + \mathcal{C}(g_{\theta_{bw}}(g_{\theta_{fw}}(\mathbf{P}^t)), \mathbf{P}^t). \quad (3)$$

For compactness, we have let $g(\mathbf{X}) = f(\mathbf{X}) + \mathbf{X}$ and \mathcal{C} be the truncated symmetric chamfer distance as described in [43]. We differ from the original method in that we do not use ℓ_2 regularization on the weights. We find that when combined with motion compensation that regularization leads to zero flow predictions everywhere.

Rigid Refinement: Piecewise rigidity has been a common choice of prior for scene flow estimation and has been widely used for LiDAR scene flow [20, 15]. In contrast to recent learning-based methods which require differentiable rigid refinement for loss functions, we can robustly fit a piecewise rigid model to the flow estimates produced by the previous step. First we use DBSCAN [17] to produce a set of clusters $\{\mathcal{V}_j = \{\mathbf{p}_k\}_{k=1}^K\}_{j=1}^J$. Then for each cluster, we use RANSAC [18] to fit a rigid model to flow predictions for that cluster. That is for each RANSAC iteration we randomly sample 3 points $\mathbf{p}_1, \mathbf{p}_2, \mathbf{p}_3$ (the minimum required to get a unique solution) and their associated flow vectors $\mathbf{f}_1, \mathbf{f}_2, \mathbf{f}_3$ and then fit rigid motion parameters by solving:

$$\min_{\mathbf{R} \in SO(3), \mathbf{t} \in \mathbb{R}^3} \sum_{i=1}^3 \|\mathbf{R}\mathbf{p}_i + \mathbf{t} - (\mathbf{p}_i + \mathbf{f}_i)\|_2^2, \quad (4)$$

with the Kabsch algorithm [34]. We then compute the norm of the difference between the raw and rigid flows, considering any below a threshold to be inliers. At the end of T iterations the rigid parameters with the highest number of inliers are selected and the parameters are recomputed with respect to the inlier set producing $\mathbf{R}^*, \mathbf{t}^*$. Since we know that with motion-compensated inputs the vast majority of flows should be zero, we further refine the flows by set-

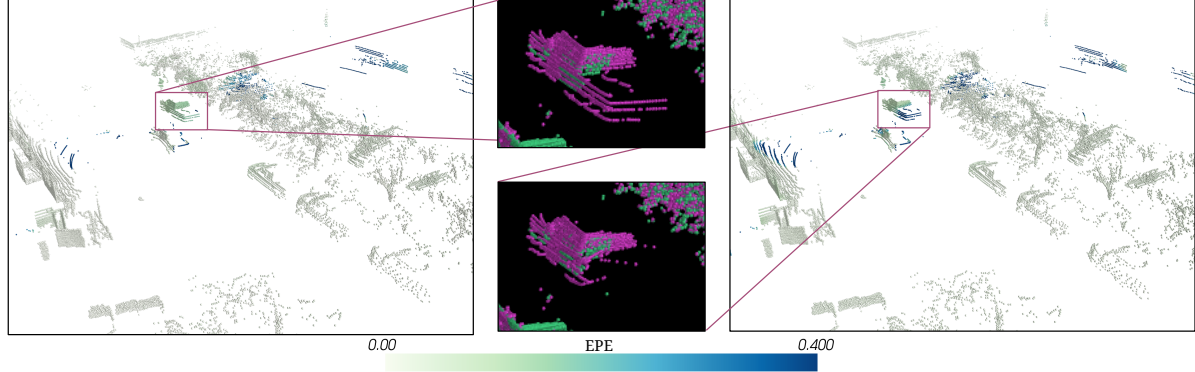


Figure 7. Optimizing for the standard nearest neighbor self-supervised loss can cause mis-predictions in the presence of strong occlusions. Here, the bed of the truck is collapsed into the cab by NSFP (left). Our RANSAC non-rigid refinement step can fix this type of error (right).

Supervision	EPE			AccR		AccS	
	Avg	Dynamic		Dynamic	Dynamic		Dynamic
		FG	Static		FG	BG	
Gojcic [20]	Weak	0.083	0.155	0.064	0.032	0.650	0.368
EgoFlow [70]	Weak	0.205	0.447	0.079	0.090	0.111	0.018
Sim2Real [32]	Synth	0.157	0.229	0.106	0.137	0.565	0.254
PPWC [79]	Self	0.130	0.168	0.092	0.129	0.556	0.229
FlowStep3D [37]	Self	0.161	0.173	0.132	0.176	0.553	0.248
Odometry	None	0.198	0.583	0.010	0.000	0.108	0.002
ICP [10]	None	0.204	0.557	0.025	0.028	0.112	0.015
NSFP [43]	None	0.088	0.193	<u>0.033</u>	0.039	0.542	0.327
Ours	None	0.055	0.105	<u>0.033</u>	0.028	0.777	0.537

Table 2. Quantitative results on our Argoverse 2 benchmark. Our method significantly outperforms all of the existing methods on the three-way average EPE, dynamic EPE, and both accuracy measures despite not using any training data. Of particular note is the fact that we significantly outperform Gojcic *et al.* [20] which makes use of ground truth segmentation masks and ego motion for training.

	Moving		Static	50-50	
	EPE	Accuracy	Relax	EPE	EPE
Zero	0.6381	0.1632		0.5248	0.5814
ICP	0.2101	0.6151		0.0290	0.1196
PPWC	0.3539	0.2543		0.1974	0.2756
EgoFlow	0.7399	0.0000		0.0570	0.3985
SLIM (U)	0.1050	0.7365		0.0925	0.0987
Ours	0.0625	0.894		0.0660	<u>0.064</u>
SLIM (S)	<u>0.0702</u>	<u>0.8921</u>		<u>0.0499</u>	0.0600

Table 3. The results of our method on the NuScenes benchmark proposed by Baur *et al.* [5]. U and S refer to the unsupervised and fully-supervised versions of their method. Our dataless method vastly outperforms the baseline methods and even achieves comparable and superior results to the fully supervised network.

ting the rigid motion parameters to the identity transform if $\|\mathbf{t}^*\|_2$ is below a threshold. Then all points in the cluster are assigned the flow $\mathbf{f}_i = \mathbf{R}^* \mathbf{p}_i + \mathbf{t}^* - \mathbf{p}_i$. Points that were not assigned to any cluster by DBSCAN have their predictions unchanged. The effect of this step can be seen in Fig. 7.

5. Evaluation

We claim that use of the popular benchmarks is causing leading methods to degrade in quality when evaluated on real-world data. We show this by evaluating a suite of top self- and weakly-supervised models on our benchmark (5.1). We find that our dataless method outperforms all existing methods regardless of supervision. The superior performance is further confirmed on existing benchmarks (5.3). We also examine how the unrealistic rate of dynamic points present in popular benchmarks has led researchers to abandon ICP in favor of learned techniques (5.2). Finally, we evaluate our ground segmentation method (5.4).

5.1. Argoverse 2 Benchmark

Evaluation Metrics: We use a set of standard metrics:

- **EPE:** Average end-point-error *i.e.* the ℓ_2 norm of the difference between predicted and ground truth flow.
- **Accuracy Relax:** Ratio of predictions with absolute EPE less than 0.1m or relative error below 0.1.
- **Accuracy Strict:** Same as Accuracy Relax but with a threshold of 0.05.

Rather than averaging these metrics over the entire dataset, we break them into three classes of points: dynamic foreground, static foreground, and static background. Points are considered belonging to the foreground if they are contained in the bounding box of some tracked object and they are considered dynamic if they have a flow magnitude of at least 0.5 m s^{-1} . The choice of threshold is discussed in the supplement. Separating the metrics in this way is vital due to the low ratio of dynamic to static points, without it the metrics are dominated by performance on the static background. In order to produce a single number for ranking purposes we combine the EPE results on the classes into a three-way average similar to [5]. In order to save

	vehicle			pedestrian			cyclist			background
				all	moving	static	all	moving	static	all
	Ours	<u>0.35</u>	<u>0.72</u>	0.12	<u>0.52</u>	<u>0.78</u>	0.17	<u>0.55</u>	<u>0.81</u>	0.21
Jund <i>et al.</i>	0.18	0.54	0.05	0.25	0.32	0.10	0.51	0.57	0.10	0.07
Jund <i>et al.</i> (stationary)	N/A	N/A	N/A	0.90	1.30	1.13	1.24	0.06	N/A	N/A
Jablonksi <i>et al.</i>	0.47	1.27	N/A	0.62	0.88	N/A	N/A	N/A	N/A	0.09

Table 4. The error in m s^{-1} of our method compared to the *supervised* results of Jund *et al.* [33] on Waymo. In order to emphasize the need for methods not reliant on object labels, we also include their results on pedestrians and cyclists when they simulated not having annotations for those categories. We also include Jablonksi *et al.* [29] which is, to our knowledge, the only attempted replication of the original results. We include this to highlight the issues with restrictively licensed datasets such as this, and the need for the open benchmark we propose.

	Supervision	EPE	AccS	AccR
PPWC [79]	Full	0.710	0.114	0.219
FLOT [61]	Full	0.773	0.084	0.177
MeteorNet [46]	Full	0.277	/	/
Gojcic [20]	Weak	0.133	0.460	0.746
Gojcic++	Weak	0.102	0.686	0.819
Dong (Waymo Open) [15]	Weak	0.077	0.812	0.906
Dong (Semantic KITTI)	Weak	<u>0.065</u>	<u>0.857</u>	<u>0.940</u>
Ours	None	0.061	0.917	0.962

Table 5. Results of our method on lidarKITTI w/ ground [20]. We outperform all existing methods without using any training data.

computation we evaluate the methods on every 5th frame of the validation set since the performance on neighboring pairs is highly correlated. This leaves us with 5,800 test examples.

Baselines: We chose to evaluate 6 methods on our benchmark to serve as a thorough exploration of recent research. Methods were chosen if they presented a self or weakly supervised method, appeared in a recent conference, and made available a working implementation of their method. This led us to choose: PointPWC Net [79], EgoFlow [70], FlowStep3D [37], NSFP [43], Sim2Real [32], and Gojcic *et al.* [20]. Additionally, we include as baselines an off-the-shelf ICP [6] implementation [73] and the result of simply predicting the ground truth ego-motion for all points. Most of the baseline methods clip points to a depth of 35m [79, 32, 70, 37]. To make comparisons fair we only include points contained in a 70m square around the sensor as was done in [5].

Baseline Training Procedure: As much as possible we attempted to use the same training strategy as the original authors, but we also wished to enforce standardization on the amount of computing resources allocated to each method. As a result, we chose to adopt the two-stage training regime from [79]. First, we train for seven days on a quarter of the whole training set followed by five days of fine-tuning on the entire dataset. Each method was trained using the largest batch size possible on a single NVIDIA T4 GPU (some methods were not set up for multi-GPU training), and using the authors’ optimizer and learning rate schedule. Methods that were able to include

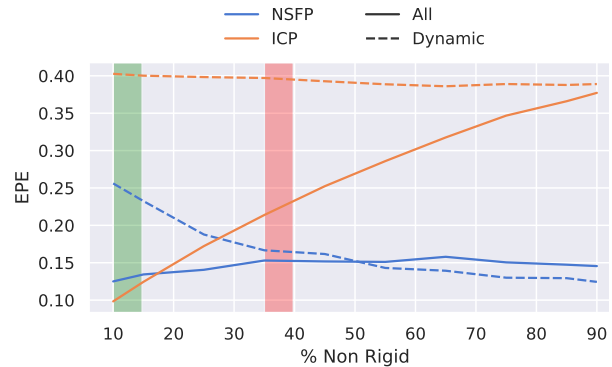


Figure 8. The performance of ICP and NSFP versus the ratio of dynamic points in each example. The green region indicates the ratio found in real data and the red region indicates the ratio found in the KITTI-SF dataset.

ground truth ego-motion in their loss formulation were also given that information. We also used ground truth foreground/background masks to train the weakly supervised method [20]. The only method that required substantial changes was [32] as its training is based on transferring information from a synthetic labeled dataset. The synthetic data comes from a virtual depth camera, so we clip the LiDAR points to match the field of view.

Results: Our results are summarized in Tab. 2. First, we can observe simply that our method outperforms all of the baselines despite not using any training data, even Gojcic *et al.* who use ground truth foreground masks. Next, we see that performance on our benchmark does not correlate with performance on the popular “real-world” KITTI-SF benchmark, validating the need for new evaluation procedures (Fig. 1). Finally, we see that essentially no method was able to match the performance of ICP at predicting the ego-motion. This is surprising since several of the methods [20, 5, 70] explicitly claim ego-motion predictions as a benefit of their architecture. Our next experiment addresses this discrepancy.

5.2. Effect of Dynamic Ratio

In order to understand why recent methods which predict ego-motion perform worse than ICP, we need to understand

how the amount of dynamic points in a scene affects the performance of ICP. We manually re-sampled each example in the validation dataset to take a specified number of dynamic and static points and then ran NSFP [43] and ICP [10]. The results can be found in Fig. 8 and show that when looking at the total EPE averaged over the entire dataset, like most evaluations, the performance of ICP steadily degrades as the percentage of dynamic points increases. At 40% dynamic points, far higher than real-world data but approximately the same ratio as KITTI-SF, ICP’s performance has degraded to significantly below the performance of NSFP. This explains why early methods which did include ICP in their comparisons [45] were able to outperform it, leading future methods to leave it out even as more realistic data became available.

5.3. Existing Benchmark Comparison

NuScenes: To further validate the performance of our method we compare with SLIM [5] the state-of-the-art self-supervised method on NuScenes. As can be seen in Tab. 3 our method vastly outperforms SLIM and the other methods they tested on the main 50-50 EPE metric, dynamic EPE, and dynamic accuracy. Again we see that ICP performs far better than every other method on static points. We also include the SLIM results when trained in a supervised manner and show that we achieve comparable and some superior results, again despite not using any training data.

Waymo: Given the dominant performance of our method as compared with self- and weakly-supervised methods, we also perform a comparison with a fully supervised approach designed to handle the large scale of Waymo, introduced in [33]. Due to the licensing of the dataset which prevents the release of trained models, we believe that ours is the only method that provides a usable baseline for other researchers. The results shown in Tab. 4 confirm the dataset author’s claims that training on more data significantly improves performance, as it performs better than the supervised SLIM network compared to ours. However, our method still shows comparable performance on many metrics. Since one goal of un-supervised flow estimation is to gain awareness of objects which are not in the tracking taxonomy, we also include the results where the authors simulated missing an object class in their labels. Our method performs significantly better in this case. We also highlight the issue of not allowing the release of trained models by including the performance of what we believe to be the only attempted replication [29], which we outperform. We note that due to the size of the validation dataset (over 30,000 examples) we evaluate our method on a random subset of 5,400 examples.

lidarKITTI: We also evaluate on lidarKITTI [20], which was generated by associating KITTI-SF labels with the raw LiDAR scans. We use the version with ground

points as ground removal is a component of our method. Ground point flow is set to the ego motion. The results are shown in Tab. 5 and further confirm the effectiveness of our approach. Our method substantially outperforms all the existing supervised methods. Additionally, we outperform the weakly supervised approaches that are optimized for use on LiDAR data and use ground truth segmentation masks. Dong *et al.* achieves similar performance, but requires training on ground truth segmentation and ego-poses. We include their results when trained on Waymo Open to highlight the sensitivity of even weakly supervised approaches to a train/test domain gap.

5.4. Ground Segmentation

We close with an evaluation of our ground segmentation method. First, we present a qualitative example (Fig. 6) showing our method effectively handling a scene with a non-planar ground. To quantitatively analyze our method we need to consider what constitutes failure. The subtlety lies in the ill-defined nature of the ground, making it impossible to define normal precision and recall metrics. Given that our goal is motion estimation, the failure we are most concerned with is classifying a dynamic point as belonging to the ground. Therefore we look at the rate at which we make this error. On NuScenes we find that 99.3% of the time points which are classified as ground are in fact static and achieve a rate of 99.4% on Waymo.

6. Conclusion

We re-examined the evaluations of self- and weakly-supervised scene flow methods in the context of autonomous driving. We found that popular benchmarks – FlyingThings3D and KITTI-SF – promote methods that perform worse on real-world data while undervaluing classical techniques. To rectify these problems we introduced a new large-scale LiDAR scene flow benchmark and proposed a dataless estimation technique that far outperformed the existing approaches. Given that our method is based on pre- and post-processing techniques, we believe that other methods not based on test-time optimization will also benefit from them.

Limitations: Our method suffers from two main drawbacks. First, the test-time optimization is quite slow, taking between 5-120s per example. However, most of the tested architectures rely on expensive nearest-neighbor-based layers, rendering them also too slow for real-time use as noted by [33]. Second is the reliance on the nearest neighbor distance for measuring the quality of flow predictions. Given the sparse nature of LiDAR point clouds, this distance is a non-ideal approximation and further improvements in self-supervised techniques will require new losses.

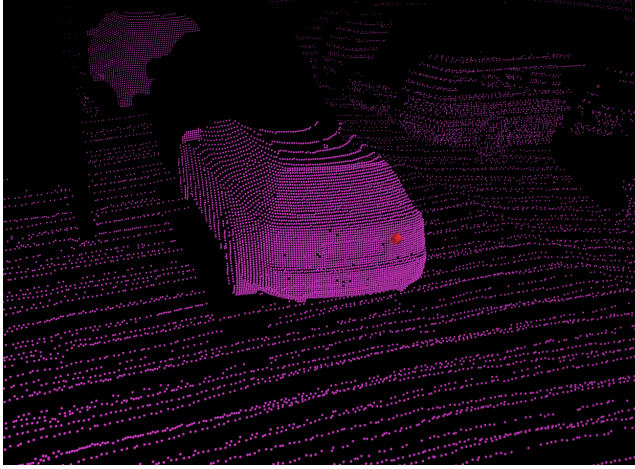


Figure 9. An example from KITTI-SF with a ball of radius 0.05 m shown in red.

A. Sampling Bias of KITTI-SF

The sampling bias of KITTI-SF makes it trivial to identify moving objects. We show that it is possible to segment KITTI-SF examples into foreground and background using only a tiny amount of local context. The much more sophisticated deep networks used for scene flow estimation can therefore also learn to identify this pattern.

Local Model: We use a “local PointNet” (Fig. 10) to predict the segmentation for a point \mathbf{p} using only the relative displacements from \mathbf{p} to all points in a local neighborhood. That is, the input to our network is the set of vectors $\{\mathbf{q} - \mathbf{p} \mid \forall \mathbf{q} \in \mathcal{N}_r(\mathbf{p})\}$ where \mathcal{N}_r is a ball of radius r centered at \mathbf{p} . We use $r = 0.05$ m in our experiment which is visualized in Fig. 9. Then we use a standard PointNet architecture to predict a binary label for the point.

Training: We train our model on the first 150 examples of KITTI-SF and test on the remaining 50. Note this is essentially the split used by FlowNet3D[45] and the recent RigidFlow[42] for fine-tuning. We train our network using a cross-entropy loss weighted by the inverse frequency of each label. We use the Adam optimizer[36] with a learning rate of 4×10^{-3} . For comparison, we perform the same experiment on real LiDAR scans from Argoverse. We sample 150 scans from the train set and 50 scans from the validation set.

Results: Using only information in a 5 cm ball around each point we are able to segment KITTI-SF with high accuracy. We achieve a mean intersection over union on the foreground of 0.83 and 0.97 on the foreground. An example is visualized in Fig. 11. In comparison when we attempt this on real LiDAR scans that do not have a biased sampling pattern, we achieve foreground and background mean intersection over union scores of 0.16 and 0.81 respectively. This demonstrates that the sampling pattern of KITTI-SF

makes it trivial to identify foreground points and should not be used for training or fine-tuning.

B. Dynamic Threshold

A key component of our evaluation was reporting the error metrics separately for dynamic and static objects. This required setting a threshold to determine which points counted as dynamic and which counted as static. Two such thresholds have been proposed in the literature: 0.5 m s^{-1} , chosen by Jund *et al.* [33] and 0.05 m s^{-1} chosen by Baur *et al.* [5]. We chose the first threshold and argue that it is significantly better than the second.

The argument rests on the distribution of the speed of dynamic objects in most LiDAR datasets, shown in Fig. 12. This distribution falls off very sharply as a function of speed (note the log scale). The result is that the average error will always be weighted mostly by points near the threshold. Consider the error metrics of a model that predicts the ground truth ego-motion for all points. If we use the 0.05 m s^{-1} threshold then in Fig. 12 the points in the yellow regions are considered static and the red and green regions are dynamic. The ego-motion model would have an average error of approximately 0 on the static points, 0.02 on points in the red region, and 0.66 on the green region. However, the exponential decrease in the number of points means that when the green and red regions are combined, the model would have an average “dynamic” EPE of approximately 0.2. This makes it seem as though a model which does not consider the dynamic motion of points at all performs reasonably well on them. In contrast, if we use the higher 0.5 m s^{-1} threshold then the ego-motion model would have a static point error of 0.01 and a dynamic error of 0.66. We believe this is a much more sensible result and choosing the higher threshold makes the error metrics much more interpretable.

C. Optimization Details

Our method uses 6 parameters which we detail here. In general the same parameters are used across all datasets (Argoverse, Waymo, NuScenes, lidarKITTI). However, due to the large variations in sparsity in both Waymo and NuScenes two parameters were adjusted: the early stopping criterion, and the DBSCAN epsilon parameter. These adjustments were not found through a parameter search, but by visually inspecting the flow results and clusters respectively.

Neural Prior Parameters: The forwards and backward flow networks have the same structure as [43] and we optimize them with the Adam[36] optimizer using a learning rate of 0.004 and no weight decay. We stop the optimization when no progress is made for 100 iterations (200 when optimizing on Waymo).

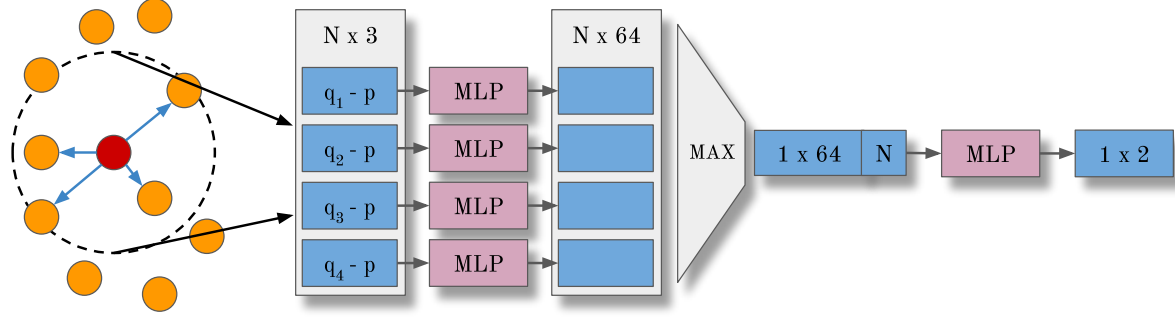


Figure 10. Our local segmentation model only uses information about the relative position of points in a local neighborhood around the predicted point. The local and global MLPs each have two hidden layers of 64 units.

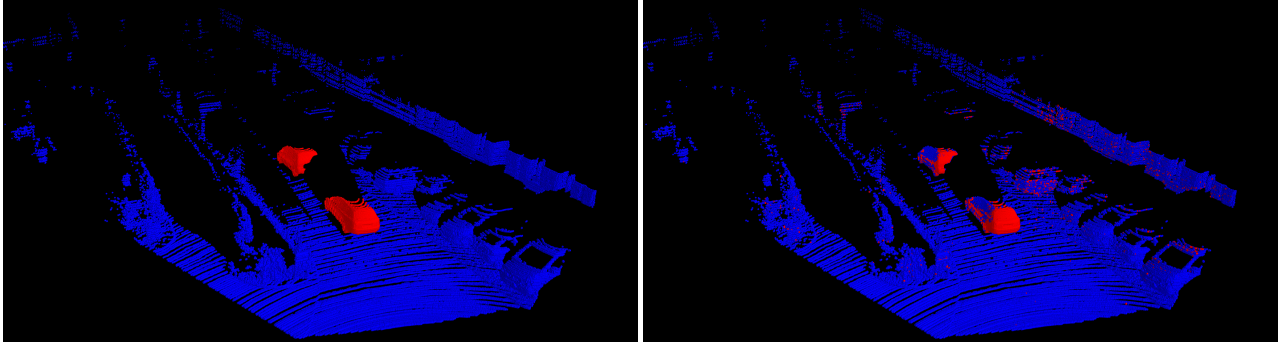


Figure 11. An example ground truth segmentation from KITTI-SF (right) compared with (left) an example prediction from our local model. Note how the model can even identify parked vs moving cars since only moving vehicles have the dense sampling pattern.

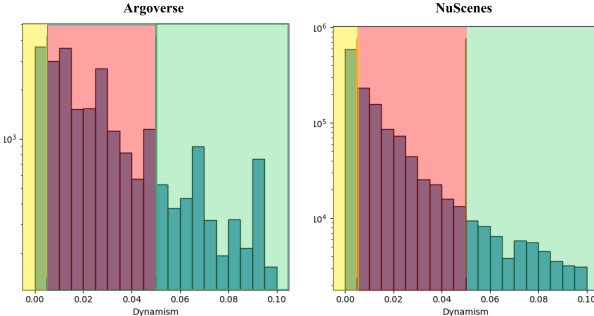


Figure 12. Distribution of the magnitude of dynamic motion for foreground points in NuScenes and Argoverse shown as a histogram. The y axis shows the log of the number of points in each bin and the x axis shows the norm of the flow vectors once ego-motion has been removed. The colored regions correspond to the two dynamic thresholds currently in use.

RANSAC Parameters: For all clusters we do 250 RANSAC iterations and we use an inlier threshold of 0.2. When thresholding on the translation component we use the same threshold as the dataset’s dynamic threshold, 0.05 for Argoverse and Waymo and lidarKITTI, and 0.005 for NuScenes.

DBSCAN Parameters: For Argoverse, Waymo and

	EPE			AccR	AccS
	Avg	Dynamic		Dynamic	Dynamic
		FG	BG		
Backbone	0.088	0.193	0.033	0.039	0.542
w/ Motion Compensation	0.066	0.112	0.042	0.046	0.756
w/ Motion & w/ Rigid Refinement	0.055	0.105	0.033	0.028	0.777
					0.537

Table 6. Ablation of the two main components of our model, motion compensation and rigid refinement.

lidarKITTI we use an epsilon parameter of 0.4 but for NuScenes we increase this to 0.8 due to the sparsity. For all datasets, we use a minimum point threshold of 10.

D. Ablation

To test the components of our method, we performed an ablation study on Argoverse. The results are shown in Tab. 6 and show that both Motion Compensation and Rigid Refinement play key roles in improving the performance of the backbone scene flow method. Motion Compensation has the largest impact on estimating dynamic motion by allowing the network to simply assign zero to background points. The rigid refinement step improves dynamic motion estimates, but also has a large impact on static points by fixing erroneous motion estimates caused by sampling artifacts.

References

[1] Brian Amberg, Sami Romdhani, and Thomas Vetter. Optimal step nonrigid icp algorithms for surface registration. In *IEEE Conf. Comput. Vis. Pattern Recog.*, pages 1–8. IEEE, 2007. 2

[2] Matan Atzmon and Yaron Lipman. Sal: Sign agnostic learning of shapes from raw data. In *IEEE Conf. Comput. Vis. Pattern Recog.*, pages 2565–2574, 2020. 2

[3] Tali Basha, Yael Moses, and Nahum Kiryati. Multi-view scene flow estimation: A view centered variational approach. *Int. J. Comput. Vis.*, 101(1):6–21, 2013. 2

[4] Ramy Battrawy, René Schuster, Mohammad-Ali Nikouei Mahani, and Didier Stricker. Rms-flownet: Efficient and robust multi-scale scene flow estimation for large-scale point clouds. In *Int. Conf. Rob. Aut.*, pages 883–889. IEEE, 2022. 2

[5] Stefan Andreas Baur, David Josef Emmerichs, Frank Moosmann, Peter Pinggera, Björn Ommer, and Andreas Geiger. Slim: Self-supervised lidar scene flow and motion segmentation. In *Int. Conf. Comput. Vis.*, pages 13126–13136, 2021. 1, 2, 3, 4, 6, 7, 8, 9

[6] Albert E Beaton and John W Tukey. The fitting of power series, meaning polynomials, illustrated on band-spectroscopic data. *Technometrics*, 16(2):147–185, 1974. 7

[7] Aseem Behl, Despoina Paschalidou, Simon Donné, and Andreas Geiger. Pointflownet: Learning representations for rigid motion estimation from point clouds. In *Int. Conf. Comput. Vis.*, pages 7962–7971, 2019. 1, 2

[8] Fabian Brickwedde, Steffen Abraham, and Rudolf Mester. Mono-sf: Multi-view geometry meets single-view depth for monocular scene flow estimation of dynamic traffic scenes. In *Int. Conf. Comput. Vis.*, pages 2780–2790, 2019. 2

[9] Holger Caesar, Varun Bankiti, Alex H Lang, Sourabh Vora, Venice Erin Liang, Qiang Xu, Anush Krishnan, Yu Pan, Giacarlo Baldan, and Oscar Beijbom. nuscenes: A multi-modal dataset for autonomous driving. In *IEEE Conf. Comput. Vis. Pattern Recog.*, pages 11621–11631, 2020. 3, 4

[10] Yang Chen and Gérard Medioni. Object modelling by registration of multiple range images. *Img. Vis. Comput.*, 10(3):145–155, 1992. 2, 4, 6, 8

[11] Zhiqin Chen and Hao Zhang. Learning implicit fields for generative shape modeling. In *IEEE Conf. Comput. Vis. Pattern Recog.*, pages 5939–5948, 2019. 2

[12] Wencan Cheng and Jong Hwan Ko. Bi-pointflownet: Bidirectional learning for point cloud based scene flow estimation. In *Eur. Conf. Comput. Vis.*, pages 108–124. Springer, 2022. 2

[13] Haili Chui and Anand Rangarajan. A new point matching algorithm for non-rigid registration. *Comput. Vis. Img. Und.*, 89(2-3):114–141, 2003. 2

[14] Ayush Dewan, Tim Caselitz, Gian Diego Tipaldi, and Wolfram Burgard. Rigid scene flow for 3d lidar scans. In *Int. Conf. Intel. Rob. Sys.*, pages 1765–1770. IEEE, 2016. 2

[15] Guanting Dong, Yueyi Zhang, Hanlin Li, Xiaoyan Sun, and Zhiwei Xiong. Exploiting rigidity constraints for lidar scene flow estimation. In *IEEE Conf. Comput. Vis. Pattern Recog.*, pages 12776–12785, 2022. 2, 5, 7

[16] Marvin Eisenberger, Zorah Lahner, and Daniel Cremers. Smooth shells: Multi-scale shape registration with functional maps. In *IEEE Conf. Comput. Vis. Pattern Recog.*, pages 12265–12274, 2020. 2

[17] Martin Ester, Hans-Peter Kriegel, Jörg Sander, and Xiaowei Xu. A density-based algorithm for discovering clusters in large spatial databases with noise. In *Int. Conf. Know. Disc. Data Min.*, KDD’96, page 226–231. AAAI Press, 1996. 5

[18] Martin A Fischler and Robert C Bolles. Random sample consensus: a paradigm for model fitting with applications to image analysis and automated cartography. *Comm. ACM*, 24(6):381–395, 1981. 5

[19] Andreas Geiger, Philip Lenz, and Raquel Urtasun. Are we ready for autonomous driving? the kitti vision benchmark suite. In *IEEE Conf. Comput. Vis. Pattern Recog.*, pages 3354–3361. IEEE, 2012. 3

[20] Zan Gojcic, Or Litany, Andreas Wieser, Leonidas J Guibas, and Tolga Birdal. Weakly supervised learning of rigid 3d scene flow. In *IEEE Conf. Comput. Vis. Pattern Recog.*, pages 5692–5703, 2021. 2, 3, 5, 6, 7, 8

[21] Xiuye Gu, Yijie Wang, Chongruo Wu, Yong Jae Lee, and Panqu Wang. Hplflownet: Hierarchical permutohedral lattice flownet for scene flow estimation on large-scale point clouds. In *IEEE Conf. Comput. Vis. Pattern Recog.*, pages 3254–3263, 2019. 2

[22] Simon Hadfield and Richard Bowden. Kinecting the dots: Particle based scene flow from depth sensors. In *Int. Conf. Comput. Vis.*, pages 2290–2295. IEEE, 2011. 2

[23] Simon Hadfield and Richard Bowden. Scene particles: Unregularized particle-based scene flow estimation. *IEEE Trans. Pattern Anal. Mach. Intell.*, 36(3):564–576, 2013. 2

[24] Michael Himmelsbach, Felix V Hundelshausen, and H-J Wuensche. Fast segmentation of 3d point clouds for ground vehicles. In *Intel. Veh. Symp. IV*, pages 560–565. IEEE, 2010. 2

[25] Michael Hornacek, Andrew Fitzgibbon, and Carsten Rother. Sphereflow: 6 dof scene flow from rgb-d pairs. In *IEEE Conf. Comput. Vis. Pattern Recog.*, pages 3526–3533, 2014. 2

[26] Peter J Huber. Robust estimation of a location parameter. In *Breakthroughs in statistics*, pages 492–518. Springer, 1992. 5

[27] Junhwa Hur and Stefan Roth. Self-supervised monocular scene flow estimation. In *IEEE Conf. Comput. Vis. Pattern Recog.*, pages 7396–7405, 2020. 2

[28] Shahram Izadi, David Kim, Otmar Hilliges, David Molyneaux, Richard Newcombe, Pushmeet Kohli, Jamie Shotton, Steve Hodges, Dustin Freeman, Andrew Davison, and Andrew Fitzgibbon. Kinectfusion: Real-time 3d reconstruction and interaction using a moving depth camera. In *User Int. Soft. Tech.*, '11, page 559–568, New York, NY, USA, 2011. Association for Computing Machinery. 2

[29] Felix Jablonski, Aron Distelzweig, and Carlos Maranes. Fastflow3d-pytorch: Implementation of the fastflow3d scene flow architecture (jund et. al 2021) in pytorch. <https://github.com/Jabb0/FastFlow3D>, 2021. 7, 8

[30] Huaizu Jiang, Deqing Sun, Varun Jampani, Zhaoyang Lv, Erik Learned-Miller, and Jan Kautz. Sense: A shared en-

coder network for scene-flow estimation. In *IEEE Conf. Comput. Vis. Pattern Recog.*, pages 3195–3204, 2019. 2

[31] Víctor Jiménez, Jorge Godoy, Antonio Artuñedo, and Jorge Villagra. Ground segmentation algorithm for sloped terrain and sparse lidar point cloud. *IEEE Access*, 9:132914–132927, 2021. 2

[32] Zhao Jin, Yinjie Lei, Naveed Akhtar, Haifeng Li, and Munawar Hayat. Deformation and correspondence aware unsupervised synthetic-to-real scene flow estimation for point clouds. In *IEEE Conf. Comput. Vis. Pattern Recog.*, pages 7233–7243, 2022. 2, 3, 4, 6, 7

[33] Philipp Jund, Chris Sweeney, Nichola Abdo, Zhifeng Chen, and Jonathon Shlens. Scalable scene flow from point clouds in the real world. *IEEE Rob. Aut. Letters*, 7(2):1589–1596, 2021. 2, 3, 4, 5, 7, 8, 9

[34] Wolfgang Kabsch. A solution for the best rotation to relate two sets of vectors. *Acta Crystallographica Section A: Crystal Physics, Diffraction, Theoretical and General Crystallography*, 32(5):922–923, 1976. 5

[35] R. Kesten, M. Usman, J. Houston, T. Pandya, K. Nadhamuni, A. Ferreira, M. Yuan, B. Low, A. Jain, P. Ondruska, S. Omari, S. Shah, A. Kulkarni, A. Kazakova, C. Tao, L. Platinsky, W. Jiang, and V. Shet. Level 5 perception dataset 2020. <https://level-5.global/level5/data/>, 2019. 4

[36] Diederik P Kingma and Jimmy Ba. Adam: A method for stochastic optimization. *arXiv preprint arXiv:1412.6980*, 2014. 9

[37] Yair Kittenplon, Yonina C Eldar, and Dan Raviv. Flowstep3d: Model unrolling for self-supervised scene flow estimation. In *IEEE Conf. Comput. Vis. Pattern Recog.*, pages 4114–4123, 2021. 2, 6, 7

[38] Alex H Lang, Sourabh Vora, Holger Caesar, Lubing Zhou, Jiong Yang, and Oscar Beijbom. Pointpillars: Fast encoders for object detection from point clouds. In *IEEE Conf. Comput. Vis. Pattern Recog.*, pages 12697–12705, 2019. 2

[39] Seungjae Lee, Hyungtae Lim, and Hyun Myung. Patchwork++: Fast and robust ground segmentation solving partial under-segmentation using 3d point cloud. In *Int. Conf. Intel. Rob. Sys.*, pages 13276–13283. IEEE, 2022. 2

[40] Hao Li, Robert W Sumner, and Mark Pauly. Global correspondence optimization for non-rigid registration of depth scans. In *Comput. Graph. For.*, volume 27, pages 1421–1430. Wiley Online Library, 2008. 2

[41] Ruibo Li, Guosheng Lin, Tong He, Fayao Liu, and Chunhua Shen. Hcrf-flow: Scene flow from point clouds with continuous high-order crfs and position-aware flow embedding. In *IEEE Conf. Comput. Vis. Pattern Recog.*, pages 364–373, 2021. 2

[42] Ruibo Li, Chi Zhang, Guosheng Lin, Zhe Wang, and Chunhua Shen. Rigidflow: Self-supervised scene flow learning on point clouds by local rigidity prior. In *IEEE Conf. Comput. Vis. Pattern Recog.*, pages 16959–16968, 2022. 2, 9

[43] Xueqian Li, Jhony Kaezemel Pontes, and Simon Lucey. Neural scene flow prior. *Adv. Neural Inform. Process. Syst.*, 34:7838–7851, 2021. 2, 3, 4, 5, 6, 7, 8, 9

[44] Yangyan Li, Rui Bu, Mingchao Sun, Wei Wu, Xinhuan Di, and Baoquan Chen. Pointcnn: Convolution on x-transformed points. *Adv. Neural Inform. Process. Syst.*, 31, 2018. 2

[45] Xingyu Liu, Charles R Qi, and Leonidas J Guibas. Flownet3d: Learning scene flow in 3d point clouds. In *IEEE Conf. Comput. Vis. Pattern Recog.*, pages 529–537, 2019. 1, 2, 3, 4, 8, 9

[46] Xingyu Liu, Mengyuan Yan, and Jeannette Bohg. Meteoronet: Deep learning on dynamic 3d point cloud sequences. In *IEEE Conf. Comput. Vis. Pattern Recog.*, pages 9246–9255, 2019. 7

[47] Wei-Chiu Ma, Shenlong Wang, Rui Hu, Yuwen Xiong, and Raquel Urtasun. Deep rigid instance scene flow. In *Int. Conf. Comput. Vis.*, pages 3614–3622, 2019. 2

[48] Nikolaus Mayer, Eddy Ilg, Philip Hausser, Philipp Fischer, Daniel Cremers, Alexey Dosovitskiy, and Thomas Brox. A large dataset to train convolutional networks for disparity, optical flow, and scene flow estimation. In *IEEE Conf. Comput. Vis. Pattern Recog.*, pages 4040–4048, 2016. 1, 2, 3

[49] Moritz Menze and Andreas Geiger. Object scene flow for autonomous vehicles. In *Int. Conf. Comput. Vis.*, pages 3061–3070, 2015. 2, 3

[50] Moritz Menze, Christian Heipke, and Andreas Geiger. Joint 3d estimation of vehicles and scene flow. *ISPRS Annals Photo. Rem. Sens. Spat. Inf. Sci.*, 2:427, 2015. 1, 3

[51] Lars Mescheder, Michael Oechsle, Michael Niemeyer, Sebastian Nowozin, and Andreas Geiger. Occupancy networks: Learning 3d reconstruction in function space. In *IEEE Conf. Comput. Vis. Pattern Recog.*, pages 4460–4470, 2019. 2

[52] Himangi Mittal, Brian Okorn, and David Held. Just go with the flow: Self-supervised scene flow estimation. In *IEEE Conf. Comput. Vis. Pattern Recog.*, June 2020. 1, 2

[53] Frank Moosmann, Oliver Pink, and Christoph Stiller. Segmentation of 3d lidar data in non-flat urban environments using a local convexity criterion. In *Intel. Veh. Symp. IV*, pages 215–220. IEEE, 2009. 2

[54] Mahyar Najibi, Jingwei Ji, Yin Zhou, Charles R Qi, Xincheng Yan, Scott Ettinger, and Dragomir Anguelov. Motion inspired unsupervised perception and prediction in autonomous driving. In *Eur. Conf. Comput. Vis.*, pages 424–443. Springer, 2022. 2

[55] Patiphon Narksri, Eiji Takeuchi, Yoshiki Ninomiya, Yoichi Morales, Naoki Akai, and Nobuo Kawaguchi. A slope-robust cascaded ground segmentation in 3d point cloud for autonomous vehicles. In *Int. Conf. Intel. Trans. Sys.*, pages 497–504. IEEE, 2018. 2

[56] Jeong Joon Park, Peter Florence, Julian Straub, Richard Newcombe, and Steven Lovegrove. Deepsdf: Learning continuous signed distance functions for shape representation. In *IEEE Conf. Comput. Vis. Pattern Recog.*, pages 165–174, 2019. 2

[57] Mark Pauly, Niloy J Mitra, Joachim Giesen, Markus H Gross, and Leonidas J Guibas. Example-based 3d scan completion. In *Symp. Geom. Proc.*, pages 23–32, 2005. 2

[58] Jean-Philippe Pons, Renaud Keriven, and Olivier Faugeras. Multi-view stereo reconstruction and scene flow estimation with a global image-based matching score. *Int. J. Comput. Vis.*, 72(2):179–193, 2007. 2

[59] J-P Pons, Renaud Keriven, O Faugeras, and Gerardo Hernández. Variational stereovision and 3d scene flow estimation with statistical similarity measures. In *Int. Conf. Comput. Vis.*, volume 2, pages 597–597. IEEE Computer Society, 2003. [2](#)

[60] Jhony Kaesemodel Pontes, James Hays, and Simon Lucey. Scene flow from point clouds with or without learning. In *Int. Conf. 3D Vis.*, pages 261–270. IEEE, 2020. [2](#)

[61] Gilles Puy, Alexandre Boulch, and Renaud Marlet. Flot: Scene flow on point clouds guided by optimal transport. In *Eur. Conf. Comput. Vis.*, pages 527–544. Springer, 2020. [2](#), [7](#)

[62] Charles R Qi, Hao Su, Kaichun Mo, and Leonidas J Guibas. Pointnet: Deep learning on point sets for 3d classification and segmentation. In *IEEE Conf. Comput. Vis. Pattern Recog.*, pages 652–660, 2017. [2](#)

[63] Charles Ruizhongtai Qi, Li Yi, Hao Su, and Leonidas J Guibas. Pointnet++: Deep hierarchical feature learning on point sets in a metric space. *Adv. Neural Inform. Process. Syst.*, 30, 2017. [2](#)

[64] Rishav Rishav, Ramy Battrawy, René Schuster, Oliver Wasenmüller, and Didier Stricker. Deeplidarflow: A deep learning architecture for scene flow estimation using monocular camera and sparse lidar. In *Int. Conf. Intel. Rob. Sys.*, pages 10460–10467. IEEE, 2020. [2](#)

[65] Rohan Saxena, René Schuster, Oliver Wasenmüller, and Didier Stricker. Pwoc-3d: Deep occlusion-aware end-to-end scene flow estimation. In *Intel. Veh. Symp. IV*, pages 324–331. IEEE, 2019. [2](#)

[66] René Schuster, Christian Unger, and Didier Stricker. A deep temporal fusion framework for scene flow using a learnable motion model and occlusions. In *Wint. Conf. App. Comput. Vis*, pages 247–255, 2021. [2](#)

[67] Lin Shao, Parth Shah, Vikrant Dwaracherla, and Jeannette Bohg. Motion-based object segmentation based on dense rgb-d scene flow. *IEEE Rob. Aut. Letters*, 3(4):3797–3804, 2018. [2](#)

[68] Vincent Sitzmann, Julien Martel, Alexander Bergman, David Lindell, and Gordon Wetzstein. Implicit neural representations with periodic activation functions. *Adv. Neural Inform. Process. Syst.*, 33:7462–7473, 2020. [2](#)

[69] Zachary Teed and Jia Deng. Raft-3d: Scene flow using rigid-motion embeddings. In *IEEE Conf. Comput. Vis. Pattern Recog.*, pages 8375–8384, 2021. [2](#)

[70] Ivan Tishchenko, Sandro Lombardi, Martin R Oswald, and Marc Pollefeys. Self-supervised learning of non-rigid residual flow and ego-motion. In *Int. Conf. 3D Vis.*, pages 150–159. IEEE, 2020. [2](#), [6](#), [7](#)

[71] Sundar Vedula, Simon Baker, Peter Rander, Robert Collins, and Takeo Kanade. Three-dimensional scene flow. In *IEEE Conf. Comput. Vis. Pattern Recog.*, volume 2, pages 722–729. IEEE, 1999. [1](#)

[72] Sundar Vedula, Simon Baker, Peter Rander, Robert Collins, and Takeo Kanade. Three-dimensional scene flow. In *Int. Conf. Comput. Vis.*, volume 2, pages 722–729. IEEE, 1999. [2](#)

[73] Ignacio Vizzo, Tiziano Guadagnino, Benedikt Mersch, Louis Wiesmann, Jens Behley, and Cyrill Stachniss. KISS-ICP: In Defense of Point-to-Point ICP – Simple, Accurate, and Robust Registration If Done the Right Way. *IEEE Rob. Aut. Letters*, 8(2):1–8, 2023. [4](#), [7](#)

[74] Christoph Vogel, Konrad Schindler, and Stefan Roth. 3d scene flow estimation with a rigid motion prior. In *Int. Conf. Comput. Vis.*, pages 1291–1298. IEEE, 2011. [2](#)

[75] Christoph Vogel, Konrad Schindler, and Stefan Roth. Piecewise rigid scene flow. In *Int. Conf. Comput. Vis.*, pages 1377–1384, 2013. [2](#)

[76] Guangming Wang, Yunzhe Hu, Zhe Liu, Yiyang Zhou, Masayoshi Tomizuka, Wei Zhan, and Hesheng Wang. What matters for 3d scene flow network. *Eur. Conf. Comput. Vis.*, 2022. [2](#)

[77] Yi Wei, Ziyi Wang, Yongming Rao, Jiwen Lu, and Jie Zhou. Pv-raft: point-voxel correlation fields for scene flow estimation of point clouds. In *IEEE Conf. Comput. Vis. Pattern Recog.*, pages 6954–6963, 2021. [2](#)

[78] Benjamin Wilson, William Qi, Tanmay Agarwal, John Lambert, Jagjeet Singh, Siddhesh Khandelwal, Bowen Pan, Ratnesh Kumar, Andrew Hartnett, Jhony Kaesemodel Pontes, et al. Argoverse 2: Next generation datasets for self-driving perception and forecasting. In *Neur. Inform. Process. Syst. Data. Bench. Track*, 2021. [3](#), [4](#)

[79] Wenzuan Wu, Zhi Yuan Wang, Zhuwen Li, Wei Liu, and Li Fuxin. Pointpwc-net: Cost volume on point clouds for (self-) supervised scene flow estimation. In *Eur. Conf. Comput. Vis.*, pages 88–107. Springer, 2020. [1](#), [2](#), [6](#), [7](#)

[80] Dimitris Zermas, Izzat Izzat, and Nikolaos Papanikolopoulos. Fast segmentation of 3d point clouds: A paradigm on lidar data for autonomous vehicle applications. In *Int. Conf. Rob. Aut.*, pages 5067–5073. IEEE, 2017. [2](#)